Supplementary Materials

Reduction-immobilizing strategy of polymer-embedded sub-2nm Cu nanoparticles with uniform size and distribution responsible for robust catalytic reactions

Rosy Amalia Kurnia Putri[a], Wail Al Zoubi[b,*], Bassem Assfour [c], Abdul Wahab Allaf [c,d], Sudiyarmanto[a], Young Gun Ko[b,*]

[a] Research Center for Chemistry, National Research and Innovation Agency-BRIN, Building 452, KST BJ Habibie, Tangerang Selatan, Banten 15314, Indonesia
[b] Materials Electrochemistry Group, School of Materials Science and Engineering, Yeungnam University, Gyeongsan 38541, South Korea
[c] Atomic Energy Commission, Department of Chemistry, P.O. Box 6091, Damascus, Syria
[d] Arab International University, Department of Pharmaceutical Chemistry and Quality Control, Faculty of Pharmacy, Ghabaghib, Darra, Syria

*Corresponding author

E-mail address: wailalzoubi@ynu.ac.kr (W. Al Zoubi) and younggun@ynu.ac.kr (Y.G. Ko)

SUPPLEMENTARY INFORMATION

Supplementary Notes: Density Functional Theory

The Density Functional Theory (DFT) is a fundamental method in quantum chemistry and physics that allows for the calculation of the electronic structure of atoms, molecules, and solids. The theoretical framework of DFT is rooted in the Hohenberg-Kohn theorems, which laid the foundation for modern DFT by establishing the relationship between the electron density and the external potential. The key physics behind DFT can be elucidated through the following equations and concepts:

1. Hohenberg-Kohn Formulation

The Hohenberg-Kohn theorem asserts that the ground state energy of a system of interacting particles can be expressed as a functional of the electron density, denoted as

$$E[n] = T[n] + E_{int}[n] + \int dr V_{ext}(r) n(r),$$

where $T[n]$ represents the kinetic energy, $E_{int}[n]$ is the electron-electron interaction energy, and $V_{ext}(r)$ is the external potential [1].

2. Kohn-Sham Equations:

The Kohn-Sham equations are a central component of DFT, simplifying the many-body problem by introducing non-interacting auxiliary particles with effective potentials. These equations are given by:

$$\left[-\frac{\hbar^2}{2m} \nabla^2 + v_s(r) \right] \phi_i(r) = \epsilon_i \phi_i(r),$$

The electron density n(r) is then calculated as $n(r)=\sum_i f_i \phi_i(r)^2$, where f_i is the occupation of the orbital [2].

3. Exchange-Correlation Functionals:

The exchange-correlation functional plays a crucial role in DFT, accounting for the electron-electron interactions beyond the simpler approximations. The Local Density Approximation (LDA) and Gradient Expansion Approximation (GEA) are common approaches to modeling the exchange-correlation energy [3].

Supplementary Notes: Responding voltage over the time during PE

The preparation of MgO support involved high-voltage discharge to from a defective MgO surface. By the oxidation of Mg metal into MgO due to voltage-assisted electrochemical reaction, the high temperature inside the electrolyte due to high potential melted the metal surface. Subsequently, chemical ions in electrolyte and Mg ions interact with each other and migrate towards the electrolyte-metal interface to gradually form oxide layer. Supplementary Fig. S2 illustrates the change in the voltage over the time as well as the evolution of plasma discharge starting from 0 up to 300 s. When the voltage reached 254 V at around 15 s, an initial electrical breakdown occurred at the surface of Mg metal due to its inability to withstand continuous and high electrical field. During the so-called breakdown potential, a myriad of transient plasma is generated at the interface between Mg and the electrolyte, which facilitate the growth of the oxide layer corresponding to the metal substrate. The pore structure was formed in the MgO layer as a result of the high energy plasma [4,5].

Supplementary Notes: Electronic contribution of 4-NP and 4-AP

The Gaussian programs package is used to optimize the 4-NP molecules seen in Supplementary Figs. S18a-b and the electrostatic potential (ESP). DFT calculations were carried out to understand the charge distributions of the optimized molecules, and the associated charges are displayed in Supplementary Fig. S18. In order to comprehend the electronic cloud of a molecule and reactive centers of compounds, ESP mapping describes the nucleophilic and electrophilic sites in the optimized molecules in which blue areas correspond to more positively charged sites, while red shaded areas belong to more negatively charged sites. These charge distributions are in accordance with the fact that 4-NP can act as effective electron acceptor during catalytic reactions that interact with electron donor which is Cu-NPs in this study. After 4-NP was successfully reduced to 4-AP, the electron clouds were altered where 4-AP becomes more positive causing 4-AP to be easily desorbed from Cu-NPs [6].

According to the frontier molecular orbital theory, the relative chemical reactivity of a molecular system can be estimated using its highest occupied molecular orbital (HOMO) and lowest unoccupied molecular orbital (LUMO). HOMO describes the active sites for electron donation, whilst LUMO corresponds to the location of electron acceptor. Supplementary Figs. S18c-d of HOMO and LUMO illustrations of 4-NP and 4-AP with the corresponding energies, revealing that HOMO is mostly located on the electron-rich carbon atom of the aromatic ring along with the electronegative oxygen atoms of –OH and –NO_2 groups. On the other hand, LUMO is primarily delocalized over –OH group and the carbon atom bonded to it, the electron-deficient nitrogen atom of NO_2 and the connected carbon atom, as well as the two specifically neighboring carbon atom.

Supplementary Notes: Thermal stability at high temperature

To confirm the thermal stability and sintering resistance of the catalyst, calcination of the Cu@polymer loaded on porous MgO was carried out at high temperatures (60 ˚C, 90 ˚C and 120

˚C). STEM results show that the size and monodispersed of Cu NPs within polymer support remain surprisingly unchanged after high treatment at either (60 ˚C, 90 ˚C and 120 ˚C) for 2 h, respectively (Supplementary Figure S19), suggesting that this catalyst has high thermal stability. It is believed that the sintering and coarsening of Cu-PVAc layer on the MgO support surface are severely inhibited by the unique embedded structure. The STEM results showed that the Cu NPs on the polymeric surface almost unchanged (Supplementary Figure S19). Therefore, the Cu-PVAc layer catalyst prepared via R-IS exhibited exceptional sintering resistance with respect to NP size and catalytic performance.

Supplementary Figures
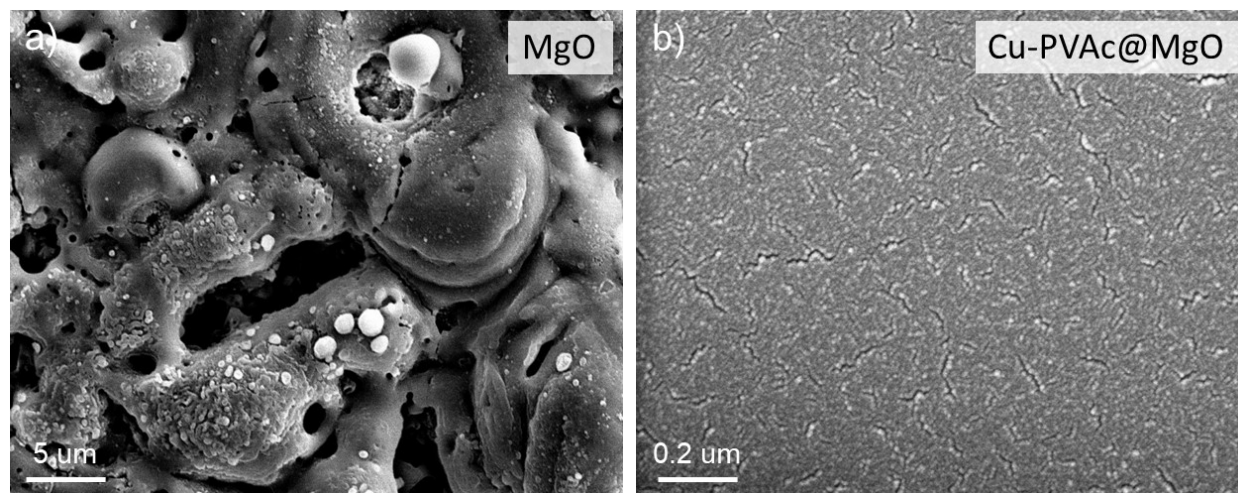
Figure S1. SEM images of (a) MgO showing the micropores to anchor Cu-PVAc layer and (b) Cu-PVAc@MgO depicting the surface of Cu-PVAc layer. However, Cu-NPs are not visible in this stage.
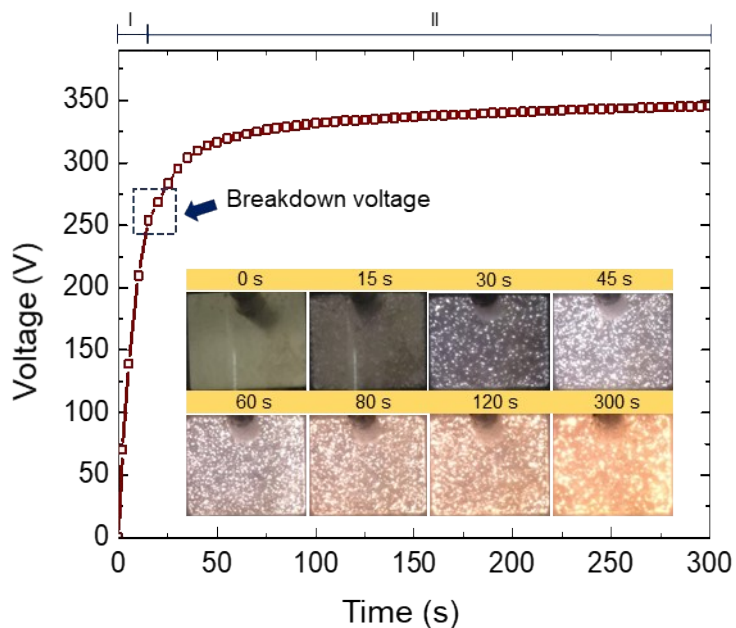
Figure S2. Responding voltage vs time curves of the substrate in the silicate-based electrolyte during PE at 100 mA cm^{-2}. The voltage linearly increased in region I as a result of passivation layer prior to reaching breakdown voltage. As the breakdown voltage was achieved due to the electron avalanche, formation of MgO support layer occurred in region II. The intensity of plasma discharges were intensified along with the reaction time.
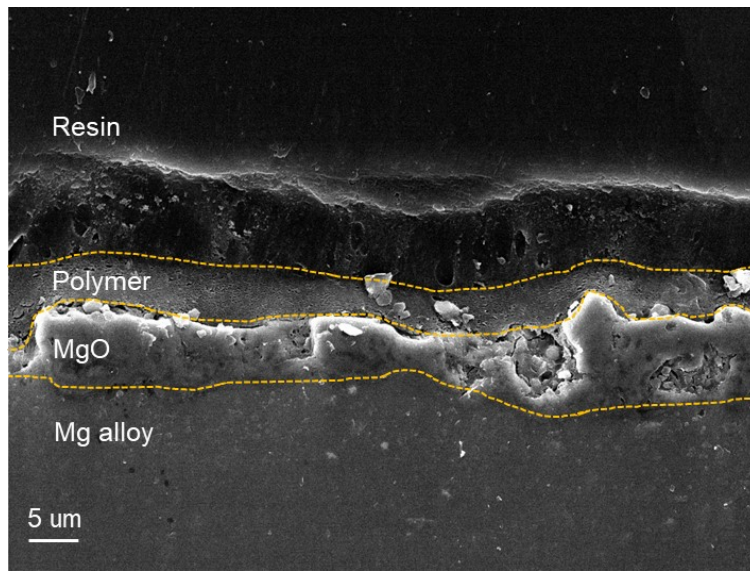
Figure S3. SEM cross-sectional morphology of Cu-PVAc@MgO showing each corresponding layer; Mg alloy, MgO, and Cu-polymer.
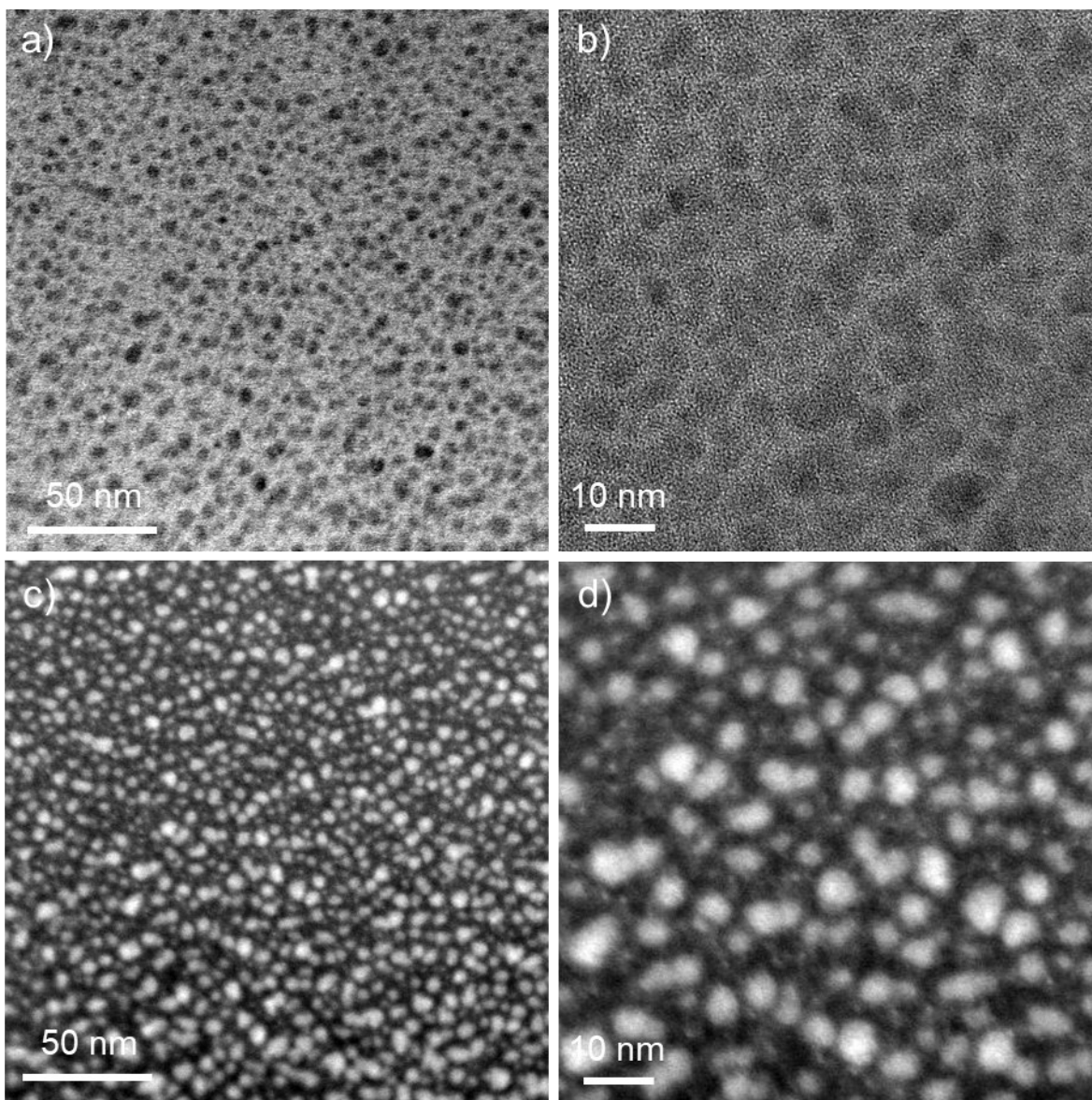
Figure S4. (a) and (b) FE-TEM images of Cu-NPs embedded in PVAc. (c) and (d) HAADF-STEM images of Cu-NPs embedded in PVAc.
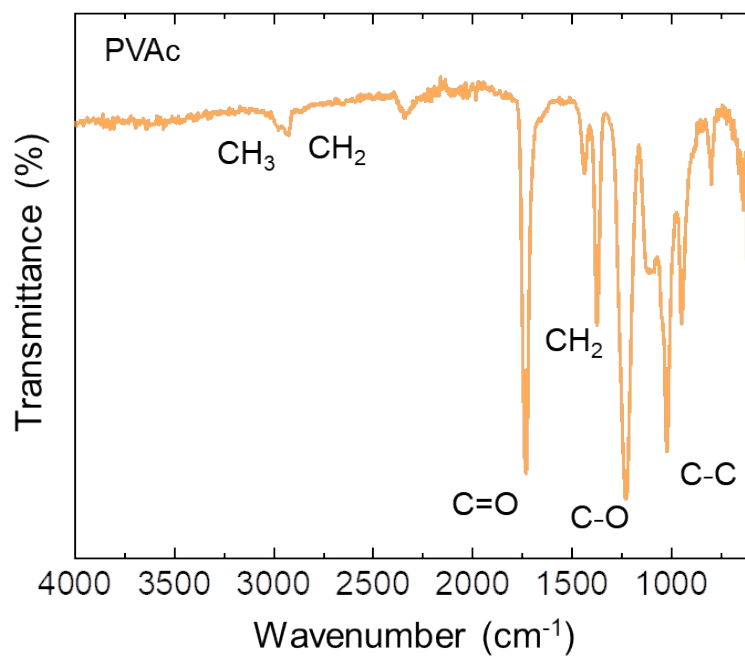
Figure S5. Fourier transform infrared (FT-IR) spectra of polyvinyl acetate, showing the peaks of functional groups in the polymer.
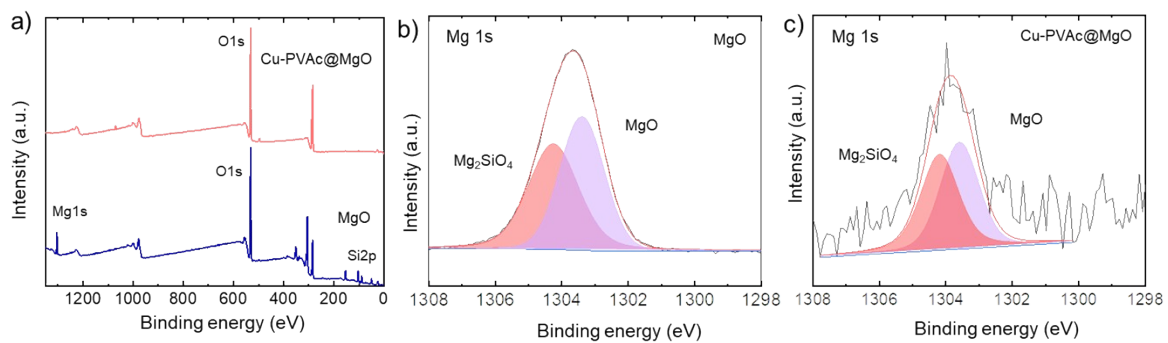
Figure S6. Chemical composition of Cu-PVAc@MgO showing (a) Survey profile of XPS. Deconvolution XPS spectra at the core level of (b) MgO and (c) Cu-PVAc@MgO.
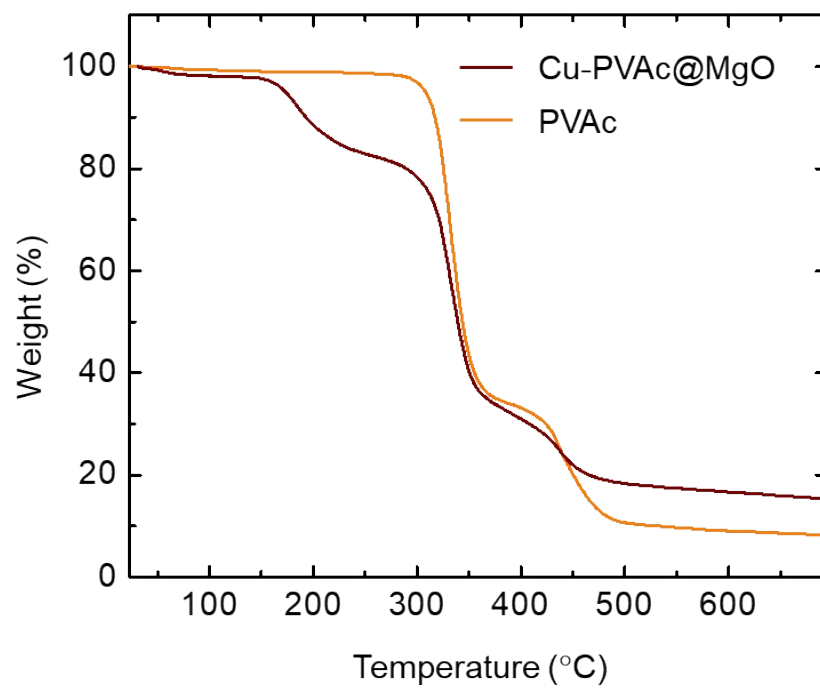
Figure S7. Thermal stability of Cu-PVAc@MgO and PVAc showing a gradually weight loss at constant heating rate of 10 °C min^{-1} with an increasing temperature by Thermogravimetric analysis (TGA).
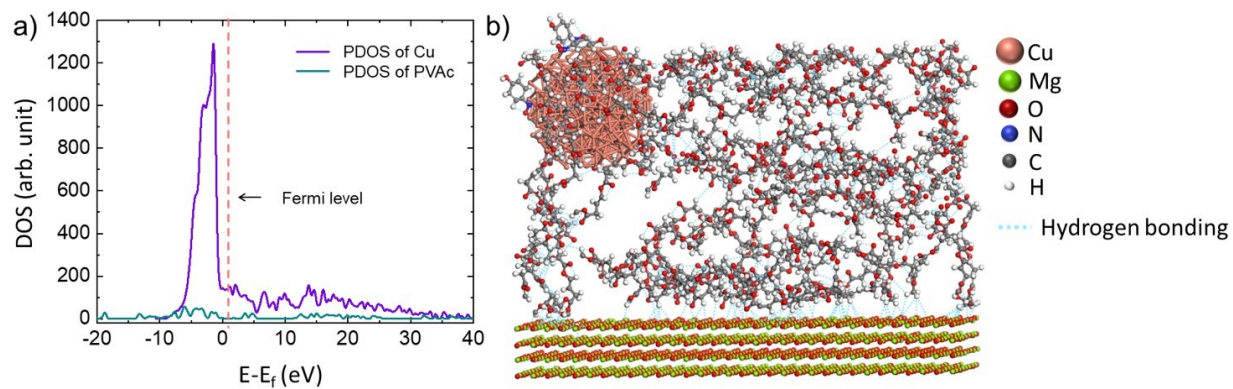
Figure S8. Computational interpretation of the interaction mechanism between Cu nanoparticles and polymer, (a) density of states (DOS) showing each molecular contributions and (b) the hydrogen bonding illustrated by blue dash line constructed the interaction between Cu nanoparticles, polymer, and MgO layer.
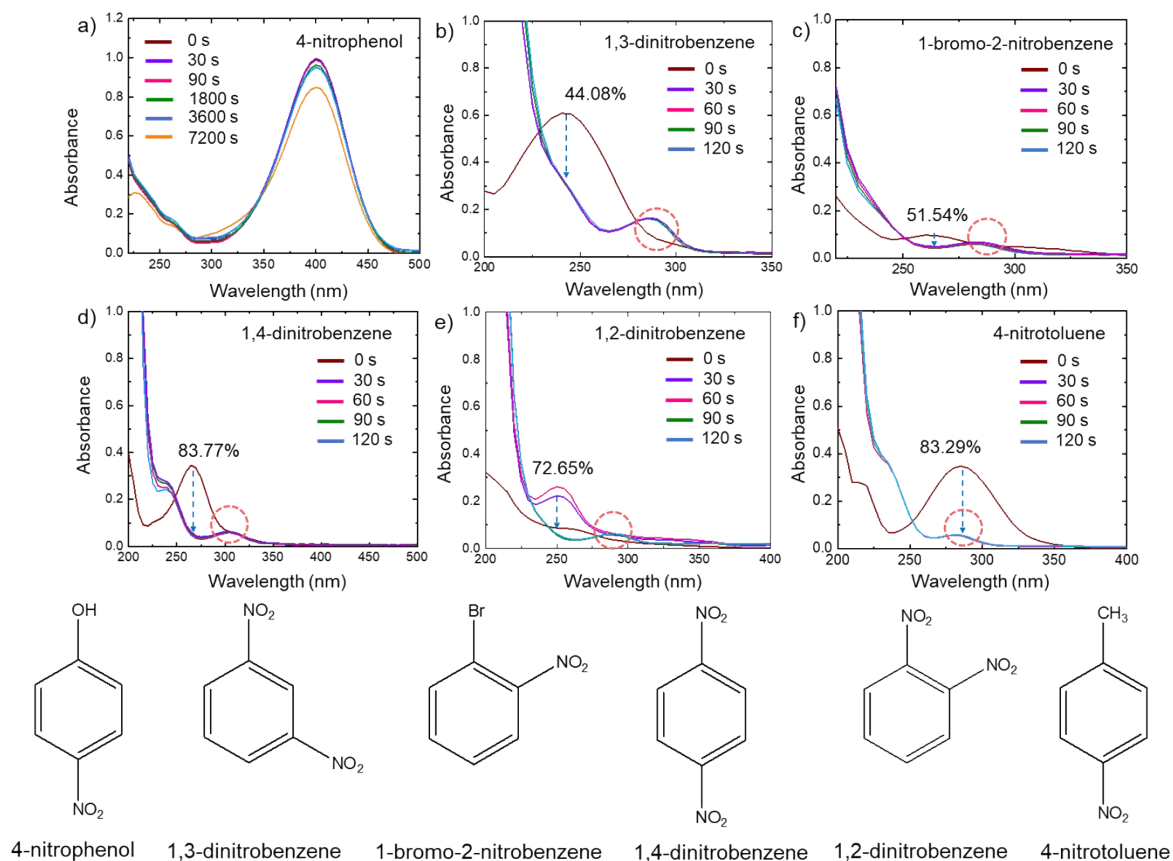
Figure S9. Ultraviolet-visible (UV-Vis) absorbance spectra of various chemical compounds: (a) 4-nitrophenol with the presence of MgO. Absorbance profile of (b) 1.3-dinitrobenzene, (c) 1-bromo-2-nitrobenzene, (d) 1.4-dinitrobenzene, (e) 1.2-dinitrobenzene, and (f) 4-nitrotoluene with the presence of Cu-PVAc@MgO catalyst.
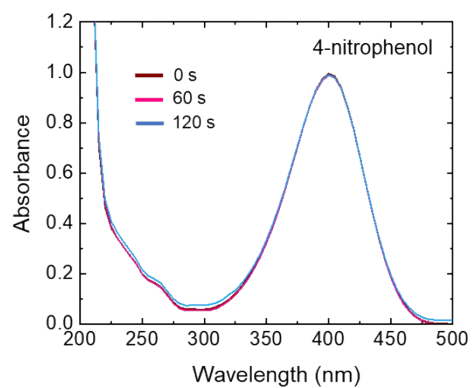
Figure S10. Ultraviolet-visible (UV-Vis) absorbance spectra of 4-nitrophenol upon MgO-PVAc layer without Cu NPs.
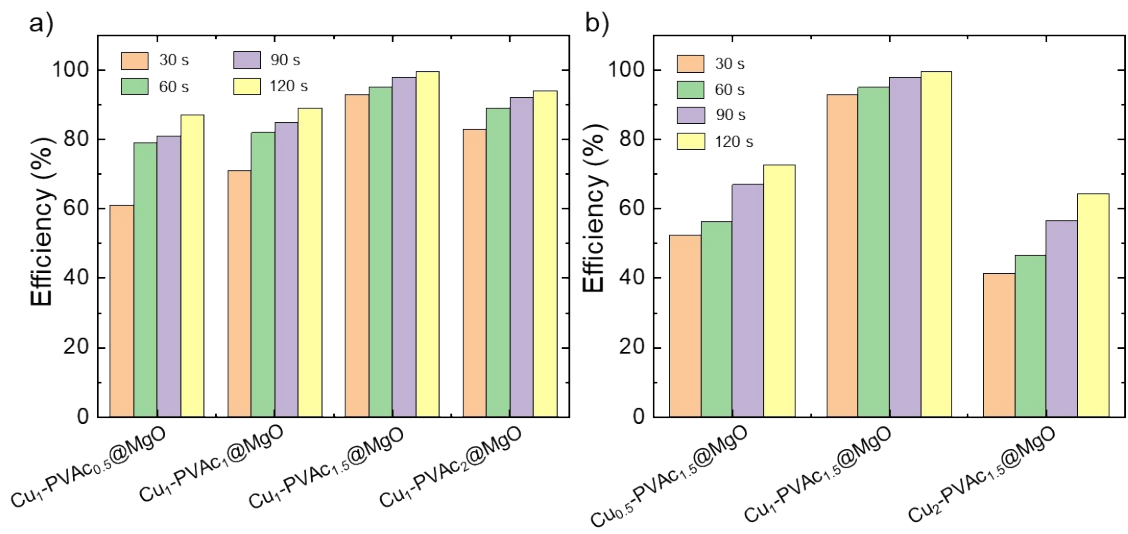
Figure S11. Efficiency of Cu-PVAc@MgO in different mol ratio of (a) PVAc and (b) Cu.
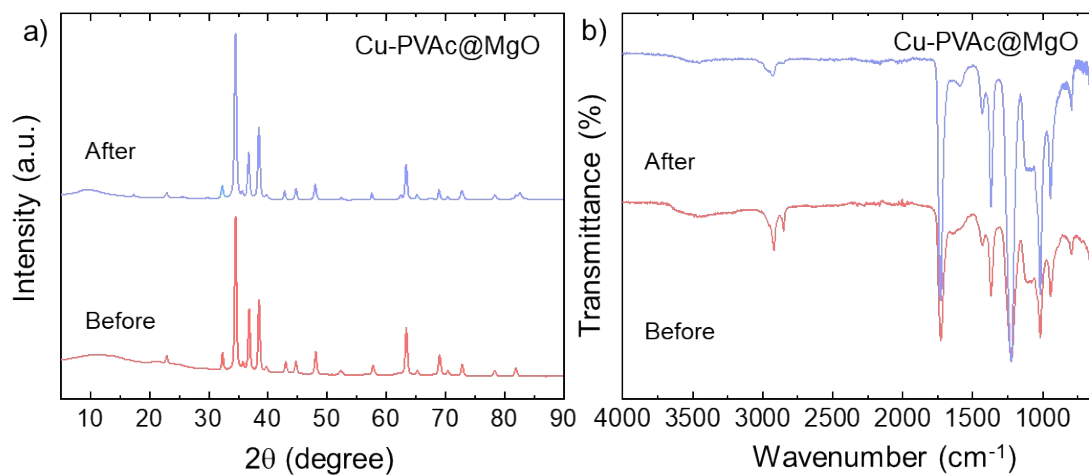
Figure S12. (a) XRD and (b) FTIR spectra of Cu-PVAc@MgO before and after fifteen cycles of catalytic reduction.

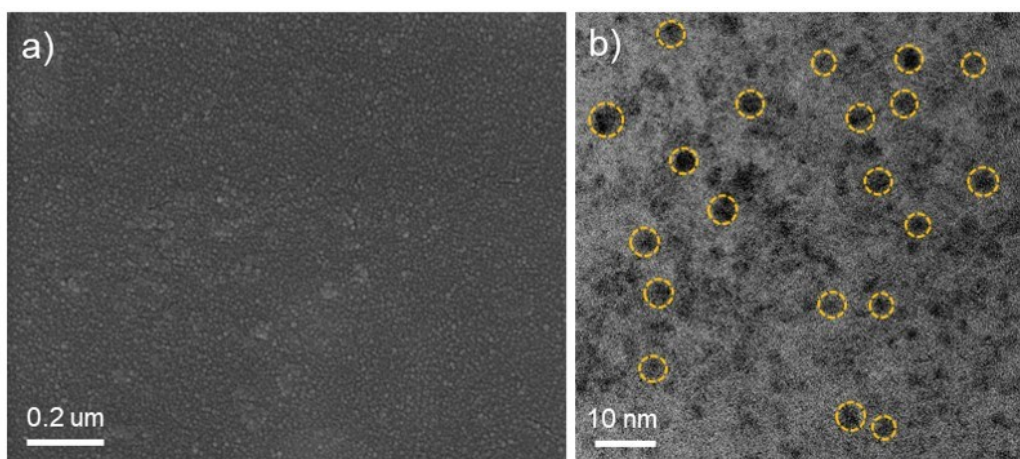**Figure S13.** (a) SEM and (b) TEM images showing morphologies of Sub-2nm Cu-PVAc@MgO after 15 consecutive cycles reduction of 4-NP
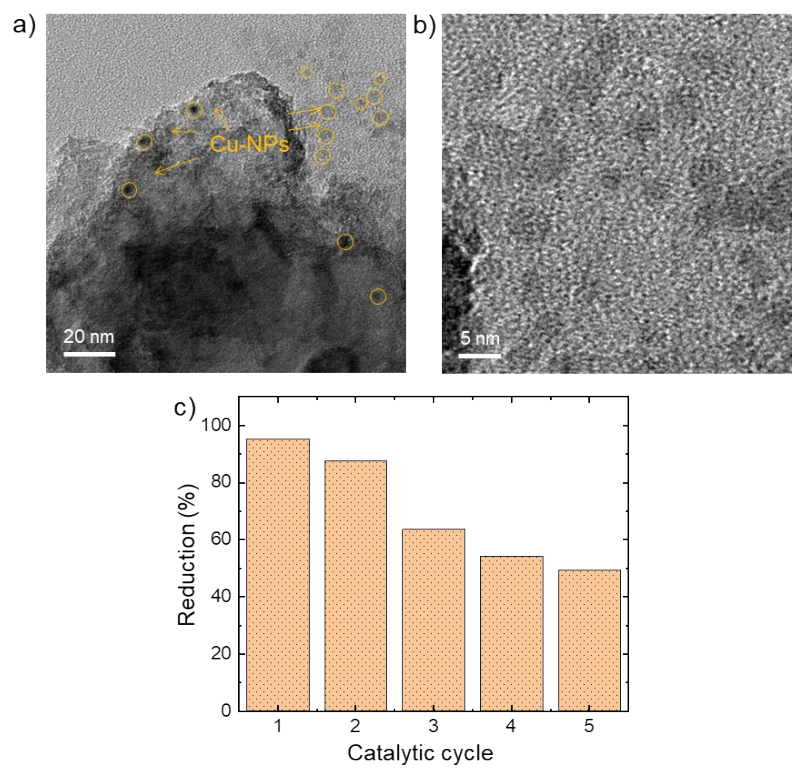
Figure S14. (a) TEM image of Cu-NPs directly deposited on MgO layer and (b) respective reduction efficiency in five consecutive cycles.
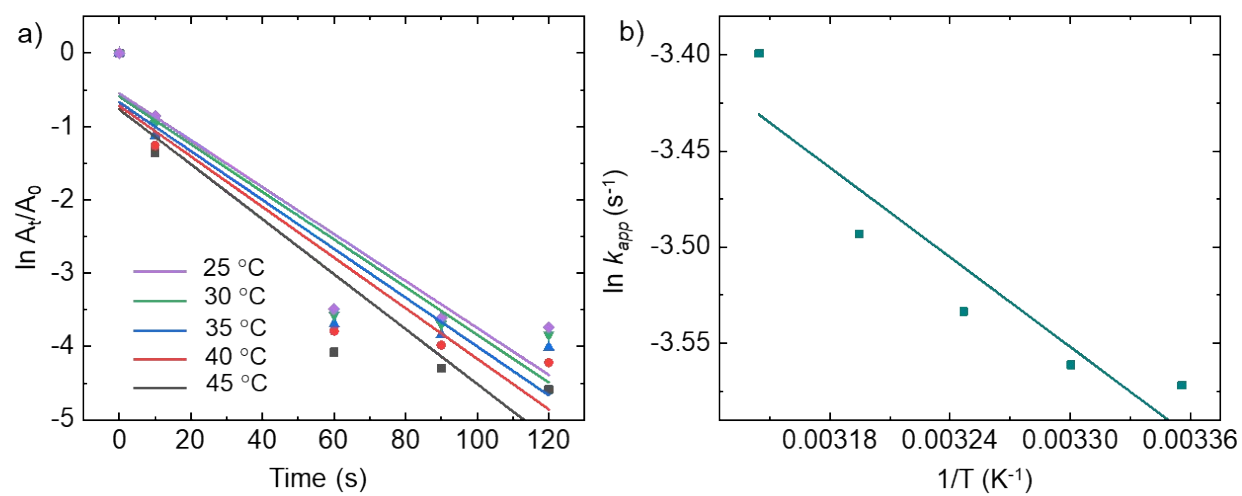
Figure S15. (a) Plot of $\ln(C_t/C_0)$ and (b) activation energy (E_a) in several temperature condition during catalytic reduction ranging from 298 to 318 K.
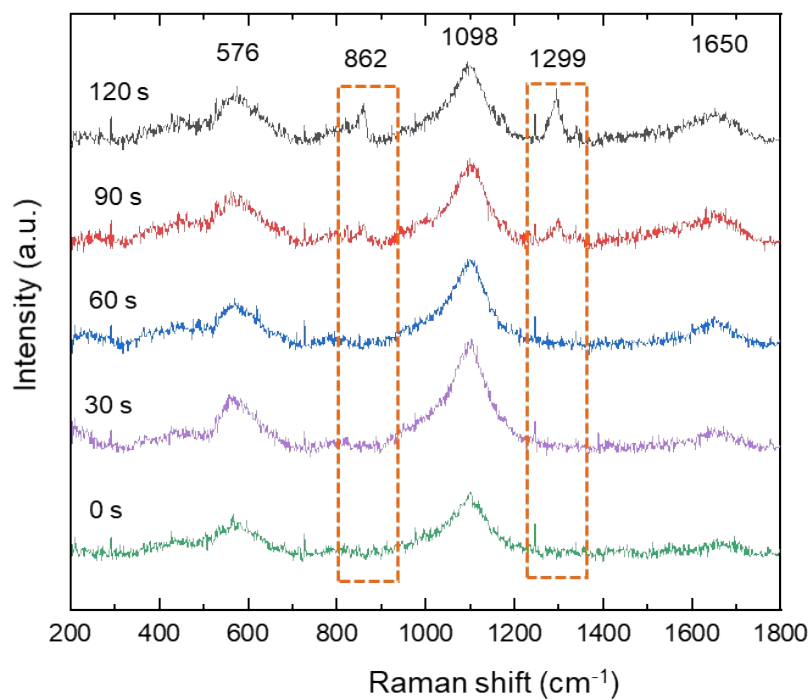
Figure S16. *In-situ* Raman spectra illustrating the conversion of 4-NP to 4-AP. The formation of new peaks marked in dash line depict the N–H vibration signal, indicating the successful reduction reaction.
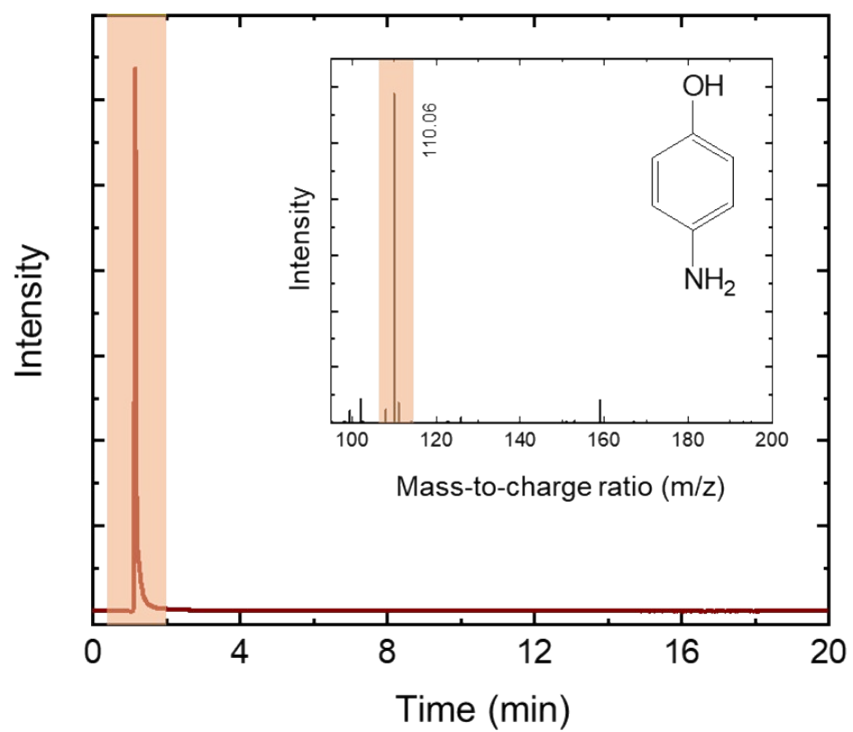
Figure S17. Confirmation of the products by a) liquid chromatography (LC) showing the single peak of 4-NP and b) mass spectrometry (MS) depicting the mass-to-charge ratio of 4-AP.
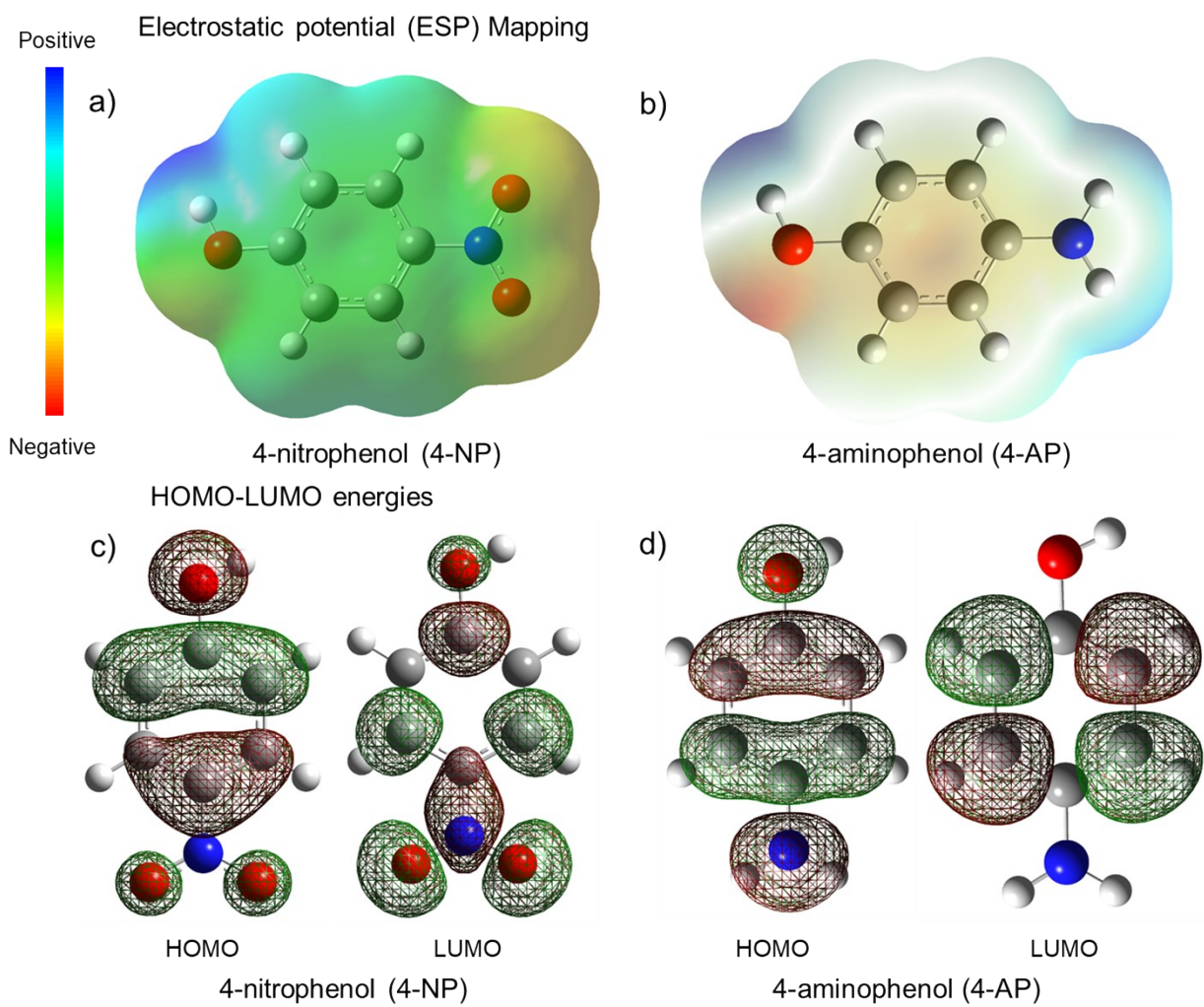
Figure S18. Electrostatic potential (ESP) mapping of (a) 4-NP and (b) 4-AP. HOMO and LUMO molecular orbitals of (c) 4-NP and (d) 4-AP.
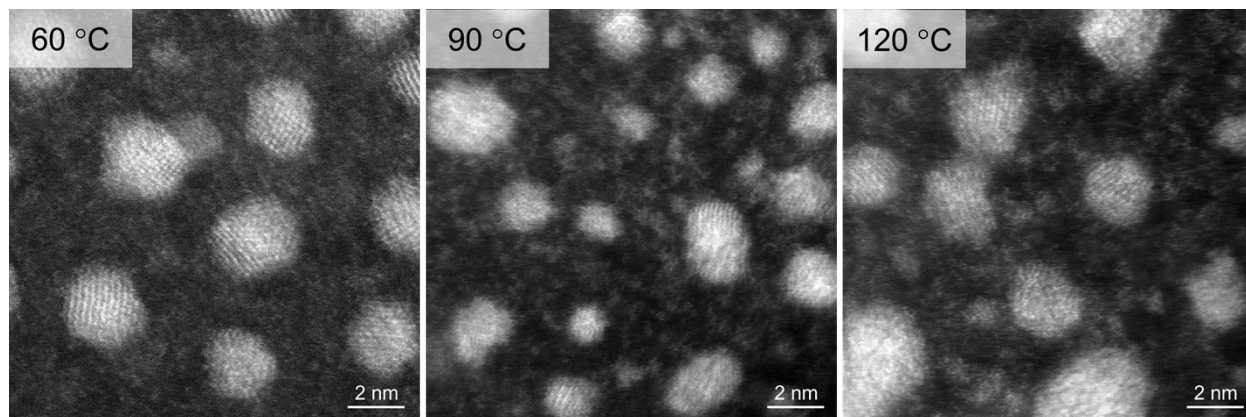
Figure S19. Microstructural observation of Cu-PVAc@MgO of three different temperatures during calcination at 60 ˚C, 90 ˚C, and 120 ˚C.

Supplementary Table

Table S1. HOMO and LUMO energies and the corresponding energy gap from 4-NP and 4-AP.

Compound	HOMO (eV)	LUMO (eV)	Energy gap (eV)
4-NP	-7.1348	-2.7608	4.374
4-AP	-4.8136	0.0179	4.831

Table S2. Comparison showing catalytic performance during reduction of 4-NP over Cu-PVAc@MgO and those Cu-based catalysts.

Catalyst	Efficiency (%)	Reaction time (minutes)	Ref.
Cu NPs/straw graphene	98	10	[7]
Cu NPs/ZSM-5	100	10	[8]
Cu NPs/Fe3O4@SiO2/EP.EN.EG	98	15	[9]
SMt@COF@Cu	95	8	[10]
Cu-Ni/C	90	5	[11]
Cu-CNT	98	6	[12]
Cu NPs	99	15	[13]
CNF/PEI-Cu	99	50	[14]
Cu@chitosan	70	27	[15]
Cu@Noria-GO	21	15	[16]
Cu-PVAc@MgO	99	0.5	This work

Table S2. Comparison of 4-NP reduction by NaBH$_4$ over Cu-PVAc@MgO with other noble metal-based catalyst.

Catalyst	Efficiency (%)	Reaction time (minutes)	k_{app} ($\times 10^{-3}$ s^{-1})	Ref.
Pd NPs/arabinolactan	95	2	1.83	[17]
TiO$_2$ NW@hollow Ag/Pt	93	10	3.8	[18]

Pd-GA/RGO	93	5	2.00	[19]
Au NPs	99	7	2.30	[20]
Au@RCC	99	10	3.00	[21]
SiO2-g-P4VP/AuNPs	99	12	2.90	[22]
Ag NPs-Co_3O_4	99	20	2.03	[23]
Ag NPs	99	9	2.80	[24]
Ag NPs	99	60	1.40	[25]
Ppy NTs-Ru	99	21	1.20	[26]
Cu NPs	99	100	1.60	[27]
Ag-Cu NPs@PP	99	14	2.4	[28]
Cu-PVAc@MgO	99	0.5	4.2	This work

Supplementary references

[1] K. Fukushima, Journal of Physics and Chemistry of Solids Excited-state theorem in both case of a nuclear potential and a more general external potential in correspondence to the Hohenberg-Kohn theorem, J. Phys. Chem. Solids. 161 (2022) 110406. https://doi.org/10.1016/j.jpcs.2021.110406.

[2] K. Dft, C. Lin, V. Gavini, TTDFT : A GPU accelerated Tucker tensor DFT code for large-scale, Comput. Phys. Commun. 282 (2023) 108516. https://doi.org/10.1016/j.cpc.2022.108516.

[3] S. Amounas, A. Hbab, L.A. Lamine, H. Chaib, T. Ait-taleb, Physica B : Condensed Matter Dependence of tetragonal barium titanate spontaneous polarization and refractive indices on DFT exchange-correlation functionals, Phys. B Condens. Matter. 674 (2024) 415536. https://doi.org/10.1016/j.physb.2023.415536.

[4] T. Suhartono, F. Hazmatulhaq, Y. Sheng, A. Chaouiki, M.P. Kamil, Y.G. Ko, In-situ construction of grass-like hybrid architecture responsible for extraordinary corrosion performance: Experimental and theoretical approach, Nano Mater. Sci. (2023). https://doi.org/10.1016/j.nanoms.2023.05.004.

[5] R.A.K. Putri, N. Nashrah, D.I. Han, W. Al Zoubi, Y.G. Ko, Chemical incorporation of Mn3O4 into TiO2 coating by benzotriazole working as electron donor: Electrochemical and catalytic performance, Compos. Part B Eng. 232 (2022) 109609. https://doi.org/10.1016/j.compositesb.2021.109609.

[6] L. Qin, W. Chen, C. Lai, S. Liu, Y. Fu, H. Yan, F. Xu, D. Ma, A. Duan, H. Deng, Q. Yang, Y. Sun, H. Ye, W. Chen, Highly efficient reduction of nitrophenols by Fe-N-C single-atom catalyst: Performance and mechanism insights, J. Environ. Chem. Eng. 11 (2023) 110278. https://doi.org/10.1016/j.jece.2023.110278.

[7] H. Dan, Y. Song, Y. Xu, Y. Gao, W. Kong, Y. Huang, Q. Yue, B. Gao, Green synthesis of Cu nanoparticles supported on straw-graphene composite for catalytic reduction of p-nitrophenol, J. Clean. Prod. 283 (2021) 124578. https://doi.org/10.1016/j.jclepro.2020.124578.

[8] S. Aslam, F. Subhan, M. Waqas, Y. Zifeng, M. Yaseen, M. Naeem, Cu nanoparticles confined within ZSM-5 derived mesoporous silica (MZ) with enhanced stability for catalytic hydrogenation of 4-nitrophenol and degradation of azo dye, Microporous Mesoporous Mater. 354 (2023) 112547. https://doi.org/10.1016/j.micromeso.2023.112547.

[9] M. Rajabzadeh, H. Eshghi, R. Khalifeh, M. Bakavoli, Generation of Cu nanoparticles on novel designed Fe3O4@SiO2/EP.EN.EG as reusable nanocatalyst for the reduction of nitro compounds, RSC Adv. 6 (2016) 19331–19340. https://doi.org/10.1039/c5ra26020e.

[10] F. Wang, F. Pan, G. Li, P. Zhang, N. Wang, Construction of spherical montmorillonite supported Cu-based catalyst doping with a covalent organic framework for 4-nitrophenol removal, Appl. Clay Sci. 214 (2021) 106278. https://doi.org/10.1016/j.clay.2021.106278.

[11] T. Kamal, A.M. Asiri, N. Ali, Catalytic reduction of 4-nitrophenol and methylene blue pollutants in water by copper and nickel nanoparticles decorated polymer sponges,

Spectrochim. Acta - Part A Mol. Biomol. Spectrosc. 261 (2021) 120019. https://doi.org/10.1016/j.saa.2021.120019.

[12]   T. Yang, Y. Tang, L. Liu, Y. Gao, Y. Zhang, Cu-anchored CNTs for effectively catalytic reduction of 4-nitrophenol, Chem. Phys. 533 (2020) 110738. https://doi.org/10.1016/j.chemphys.2020.110738.

[13]   A.K. Sasmal, S. Dutta, T. Pal, A ternary Cu2O-Cu-CuO nanocomposite: A catalyst with intriguing activity, Dalt. Trans. 45 (2016) 3139–3150. https://doi.org/10.1039/c5dt03859f.

[14]   S. Oh, H. Yu, Y. Han, H.S. Jeong, H.J. Hong, 3-D porous cellulose nanofibril aerogels with a controllable copper nanoparticle loading as a highly efficient non-noble-metal catalyst for 4-nitrophenol reduction, Chemosphere. 301 (2022) 134518. https://doi.org/10.1016/j.chemosphere.2022.134518.

[15]   W.L. Tan, N.H.H. Abu Bakar, M. Abu Bakar, Catalytic reduction of p-nitrophenol using chitosan stabilized copper nanoparticles, Catal. Letters. 145 (2015) 1626–1633. https://doi.org/10.1007/s10562-015-1547-y.

[16]   A.N. Alqhobisi, M.S. Alhumaimess, I.H. Alsohaimi, H.M.A. Hassan, A.A. Essawy, M.R. El-Aassar, H. Kalil, Efficient nitrophenol reduction with Noria-GO nanocomposite decorated with Pd–Cu nanoparticles, Environ. Res. 231 (2023) 116259. https://doi.org/10.1016/j.envres.2023.116259.

[17]   A.J. Kora, L. Rastogi, Green synthesis of palladium nanoparticles using gum ghatti (Anogeissus latifolia) and its application as an antioxidant and catalyst, Arab. J. Chem. 11 (2018) 1097–1106. https://doi.org/10.1016/j.arabjc.2015.06.024.

[18]   L. Jiang, W. Zhu, C. Wang, W. Dong, L. Zhang, G. Wang, B. Chen, C. Li, X. Zhang, Preparation of hollow Ag/Pt heterostructures on TiO2 nanowires and their catalytic properties, Appl. Catal. B Environ. 180 (2016) 344–350. https://doi.org/10.1016/j.apcatb.2015.06.033.

[19]   A.T.E. Vilian, S.R. Choe, K. Giribabu, S.C. Jang, C. Roh, Y.S. Huh, Y.K. Han, Pd nanospheres decorated reduced graphene oxide with multi-functions: Highly efficient catalytic reduction and ultrasensitive sensing of hazardous 4-nitrophenol pollutant, J. Hazard. Mater. 333 (2017) 54–62. https://doi.org/10.1016/j.jhazmat.2017.03.015.

[20]   P. Ilgin, O. Ozay, H. Ozay, A novel hydrogel containing thioether group as selective support material for preparation of gold nanoparticles: Synthesis and catalytic applications, Appl. Catal. B Environ. 241 (2019) 415–423. https://doi.org/10.1016/j.apcatb.2018.09.066.

[21]   Y. Liu, H. Dong, H. Huang, W. Zong, Y.E. Miao, G. He, I.P. Parkin, F. Lai, T. Liu, Electron-Deficient Au Nanoparticles Confined in Organic Molecular Cages for Catalytic Reduction of 4-Nitrophenol, ACS Appl. Nano Mater. 5 (2022) 1276–1283. https://doi.org/10.1021/acsanm.1c03859.

[22]   X. Chen, L. Zhang, B. Xu, T. Chen, L. Hu, W. Yao, M. Zhou, H. Xu, Hairy silica nanosphere supported metal nanoparticles for reductive degradation of dye pollutants, Nanoscale Adv. 3 (2021) 2879–2886. https://doi.org/10.1039/d1na00020a.

[23]   J. Liu, J. Li, R. Meng, P. Jian, L. Wang, Silver nanoparticles-decorated-Co3O4 porous

sheets as efficient catalysts for the liquid-phase hydrogenation reduction of p-Nitrophenol, J. Colloid Interface Sci. 551 (2019) 261–269. https://doi.org/10.1016/j.jcis.2019.05.018.

[24] F. Liu, X. Liu, F. Chen, Q. Fu, Tannic Acid: A green and efficient stabilizer of Au, Ag, Cu and Pd nanoparticles for the 4-Nitrophenol Reduction, Suzuki–Miyaura coupling reactions and click reactions in aqueous solution, J. Colloid Interface Sci. 604 (2021) 281–291. https://doi.org/10.1016/j.jcis.2021.07.015.

[25] H.L. Cao, H.B. Huang, Z. Chen, B. Karadeniz, J. Lü, R. Cao, Ultrafine Silver Nanoparticles Supported on a Conjugated Microporous Polymer as High-Performance Nanocatalysts for Nitrophenol Reduction, ACS Appl. Mater. Interfaces. 9 (2017) 5231–5236. https://doi.org/10.1021/acsami.6b13186.

[26] D.M. Fernandes, M. Rocha, C. Rivera-Cárcamo, P. Serp, C. Freire, Ru single atoms and nanoparticles on carbon nanotubes as multifunctional catalysts, Dalt. Trans. 49 (2020) 10250–10260. https://doi.org/10.1039/d0dt02096f.

[27] P. Deka, R.C. Deka, P. Bharali, In situ generated copper nanoparticle catalyzed reduction of 4-nitrophenol, New J. Chem. 38 (2014) 1789–1793. https://doi.org/10.1039/c3nj01589k.

[28] X.Q. Zhang, R.F. Shen, X.J. Guo, X. Yan, Y. Chen, J.T. Hu, W. zhong Lang, Bimetallic Ag-Cu nanoparticles anchored on polypropylene (PP) nonwoven fabrics: Superb catalytic efficiency and stability in 4-nitrophenol reduction, Chem. Eng. J. 408 (2021) 128018. https://doi.org/10.1016/j.cej.2020.128018.